Equations of state and phase diagrams for dense multi-ionic mixture plasmas

Shuji Ogata, Hiroshi Iyetomi, and Setsuo Ichimaru
Department of Physics, University of Tokyo, Bunkyo-ku, Tokyo 113, Japan

Hugh M. Van Horn
Department of Physics and Astronomy and C. E. Kenneth Mees Observatory, University of Rochester, Rochester, New York 14627-0171
(Received 12 February 1993)

Equations of state for dense binary-ionic mixture (BIM) plasmas with charge ratios $R_Z \leq 4.5$ are evaluated for both fluid and solid phases on the basis of internal energies calculated by the Monte Carlo (MC) simulation method. The accuracy of the results has been confirmed through a sum-rule analysis of the free energy with respect to screening potentials at zero separation in one-component plasmas. Phase diagrams for various BIM's appropriate to white-dwarf interiors are constructed, including the effects of compressibility of the relativistically degenerate electrons. Eutectic diagrams, which result in significant chemical separation upon solidification, are predicted for BIM's with $R_Z \gtrsim 1.6$. Free energies for dense ternary-ionic mixtures are also derived for both fluid and solid phases through comparison of the corresponding MC internal energies and by a sum-rule analysis using BIM screening potentials at zero separation. We apply the results to the process of solidification of ^{12}C-^{16}O-^{22}Ne mixtures in the interiors of white dwarfs. We find that chemical separation does indeed occur at solidification, and we obtain the result that nearly pure Ne cores are formed in such white dwarfs, even though Ne is only a trace element in the mixture.

PACS number(s): 52.25.Kn, 05.70.−a, 81.30.Bx, 64.75.+g

I. INTRODUCTION

A mixture of classical charged particles embedded in a uniform background of neutralizing charges is one of the fundamental models for the dense plasmas found in the interiors of degenerate stars. Such a plasma may be called a one-component plasma [1] (OCP), a binary-ionic mixture (BIM), a ternary-ionic mixture (TIM), and so on, depending on the number of ionic species present. Dense plasmas either in laboratories or in astrophysical settings usually contain several different species of ions, either as the principal constituents or as trace elements, i.e., as impurities.

BIM and TIM models are particularly useful for applications to the interiors of degenerate stars such as white dwarfs (WD's). Most WD's are thought to be composed mainly of carbon and oxygen left by helium burning [2], and they may contain trace elements such as neon and iron [3]. The more massive WD's, which have evolved from main-sequence stars in the mass range $M = 8M_\odot$ to $10M_\odot$, are predicted [4] to form O-Ne-Mg cores, where $M_\odot = 1.99 \times 10^{33}$ g is the solar mass. The central densities and temperatures for WD's are estimated to lie in the ranges $\rho = 10^7 - 10^{10}$ g/cm^3 and $T = 10^6 - 10^8$ K. The electrons in WD's are relativistically degenerate and constitute the (nearly) uniform distribution of background charges, while the ions are strongly Coulomb coupled, since the magnitudes of their interaction energies far exceed their thermal energies.

The equation of state for the OCP has by now been calculated quite accurately through the Monte Carlo (MC) simulation method [5–7]. It has been found that an OCP with charge Ze and mass number A solidifies into a body-centered-cubic (bcc) crystal when the Coulomb coupling parameter $\Gamma \equiv (Ze)^2/(ak_BT)$ exceeds the value $\Gamma_m \approx 172 - 180$. Here $a = (4\pi n/3)^{-1/3}$ is the radius of an "ion sphere" containing one single ion, and n is the number density of ions. Thus the OCP solidifies at a temperature $T \simeq T_m$, where

$$10^{-6} T_m(\mathrm{K}) = 9.5 \left[\frac{12}{A}\right]^{1/3} \left[\frac{Z}{6}\right]^2 [10^{-8} \rho(\mathrm{g/cm^3})]^{1/3} . \quad (1)$$

For an ionic mixture with more than one species of ions, chemical separation of the mixture may occur, either at solidification [8] or in the fluid phase [9]. Ichimaru, Iyetomi, and Ogata [10] predicted an azeotropic phase diagram for C-O BIM's based on an equation of state determined from MC simulations and variational calculations; a similar—though spindle-shaped rather than azeotropic—phase diagram was obtained independently by a density-functional calculation [11]. Except for C-O BIM's with charge ratios $R_Z \equiv Z_2/Z_1 = \frac{4}{3}$, however, accurate calculations have not previously been published for the equations of state and phase diagrams of multi-ionic mixtures.

If it occurs, chemical separation of the interior of a WD will alter its subsequent thermal evolution significantly. It has been pointed out [12] that a comparison between theoretical WD cooling calculations and the observed WD luminosity function, i.e., the distribution of the numbers of field WD's as a function of luminosity, can be used to estimate the age of the galaxy. If chemical separation occurs, the release of gravitational energy

caused by settling of the heavier matter can increase the estimated ages of the WD's substantially [13,14]. For an accreting WD, chemical separation may produce a stratification of the different species, thus affecting electron-capture rates, opacities, and nuclear-fusion rates, all of which have important effects on the evolution preceding explosion as a supernova [15–17].

In this paper, we calculate the free energies for both the fluid and solid phases of multi-ionic plasmas by extensive MC simulations, and we thereby predict the phase diagrams for BIM's with charge ratios $1 \leq R_Z \leq 4.5$. For the range $1 < R_Z \lesssim 1.4$, we find that mixed solids of the two species form at solidification, and the phase diagrams are found to be of the azeotropic type. On the other hand, nearly complete chemical separation takes place upon solidification of a BIM with $R_Z \gtrsim 1.6$, which has a phase diagram of the eutectic type. Phase diagrams for BIM's with $R_Z \approx 1.5$ exhibit composite characteristics, containing elements of both eutectic and azeotropic types. We also consider TIM's appropriate to the interiors of WD's, and we find that their excess energies evaluated from MC simulations are well represented by a bilinear mixing of the BIM values. Using the free energies thus determined, which we have confirmed separately by a sum-rule analysis, we consider the solidification of C-O-Ne TIM's. Our results predict the formation of a nearly pure Ne core in such a WD, even though Ne is only present as a trace element.

In Sec. II, we first determine the equations of state for BIM's in both the fluid and solid phases, and we construct phase diagrams for various BIM's appropriate to WD interiors. Section III is devoted to an evaluation of the free energies and phase diagrams and to a preliminary investigation of the solidification process for TIM's in WD's. We end with some concluding remarks in Sec. IV. Applications of these phase diagrams to specific astrophysical problems will be published elsewhere.

II. DENSE BINARY-IONIC MIXTURES

We consider a multi-ionic mixture consisting of N_i particles of species i, with charges $Z_i e$ and mass numbers A_i, in a volume V ($i = 1,2,\ldots$). The total number of particles is $N = \sum_i N_i$, and the ordering $Z_1 < Z_2 < \cdots$ is assumed. The thermodynamic state of a mixture with charge ratios $R_{Z,ij} \equiv Z_i/Z_j$ and molar fractions $x_i = N_i/N$ is specified by the Coulomb coupling parameters

$$\Gamma_i = \frac{(Z_i e)^2}{a_i k_B T} , \tag{2}$$

where

$$a_i = \left[\frac{3Z_i}{4\pi n_e} \right]^{1/3} \tag{3}$$

is the ion-sphere radius [18] for an ion of species i, and n_e is the (uniform) number density of neutralizing electrons. The coupling parameters in Eq. (2) are mutually related, e.g., $\Gamma_j = R_{Z,ji}^{5/3} \Gamma_i$. For simplicity, we write $R_Z \equiv R_{Z,21}$ and $x \equiv x_2$ for the BIM's.

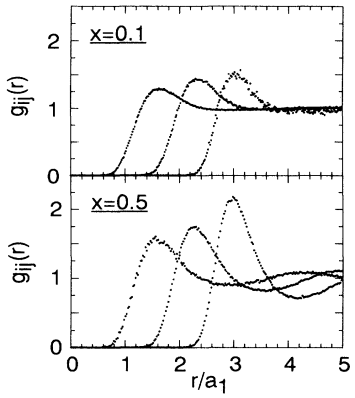

FIG. 1. MC results for the partial radial-distribution functions $g_{ij}(r)$ for BIM fluids with $R_Z = 5$ and $x = 0.1$ and 0.5. The three dotted curves in each panel correspond to the cases with ij equal to 1-1 (left), 1-2 (middle), and 2-2 (right).

A. Fluid phase

We have performed MC simulations for BIM fluids with 37 different combinations of the parameter values $R_Z = \{\frac{4}{3}, 3, 5\}$, $x = 0.01$–0.5, and $\Gamma_1 = 5$–200. We have used $N = 1000$ MC particles for cases with $R_Z = 3$ and 5, and $N = 1024$ for $R_Z = \frac{4}{3}$. In each run, 7×10^6 configurations are generated after the system has reached an equilibrated state. Figure 1 displays examples of the partial radial-distribution functions $g_{ij}(r)$ for BIM's with $R_Z = 5$ and $x = 0.1$ and 0.5 at $\Gamma_1 = 10$. The three dotted curves in each panel correspond to the pairs 1-1 (left), 1-2 (middle), and 2-2 (right). We find that the first-peak positions $r_{\mathrm{pk},ij}$ of $g_{ij}(r)$ for each pair closely follow the ion-sphere (IS) scaling; that is, $r_{\mathrm{pk},ij} \propto (a_i + a_j)/2$. Deviations from IS scaling can be seen only for the 1-1 pairs at smaller Γ_1; for $R_Z \leq 5$ and $\Gamma_1 > 5$, the deviations are adequately approximated by the expression [19]

$$\frac{r_{\mathrm{pk},11}/a_1}{r_{\mathrm{pk}}^{\mathrm{OCP}}(\Gamma_1)/a} = 1 - \frac{0.135}{\Gamma_1} \sqrt{x(R_Z - 1)} , \tag{4}$$

where we set $r_{\mathrm{pk}}^{\mathrm{OCP}}(\Gamma)/a = 1.610 + 0.025 \ln\Gamma$ as derived from the data in Ref. 6. The first peak for each pair steepens as x increases at the same Γ_1, indicating that the coupling between the lower-Z ions is in fact enhanced by the inclusion of the higher-Z ions.

The departure of $r_{\mathrm{pk},11}$ in Eq. (4) from perfect IS scaling affects the screening potentials [20,21], which are defined by

$$H_{ij}(r) = k_B T \ln g_{ij}(r) + \frac{Z_i Z_j e^2}{r} . \tag{5}$$

Our best estimates for $H_{ij}(0)$ at $R_Z \leq 5$ and $\Gamma_1 > 5$ are [19]

$$\frac{H_{ij}(0)}{k_B T}=\Gamma_{ij}(1.356-0.0213\ln\Gamma_{ij})-\frac{4(Z_i+Z_j)}{(Z_i^{1/3}+Z_j^{1/3})^3}\Gamma_{ij}(0.456-0.0130\ln\Gamma_{ij})^2(1-\Delta_{ij})^2 , \tag{6}$$

where $\Gamma_{ij}\equiv 2Z_iZ_je^2/[(a_i+a_j)k_BT]$, and the deviation from the IS-scaling value is parametrized as

$$\Delta_{ij}=\begin{cases}0.007x(R_Z-1)^2 & \text{for } (i,j)=(1,1) ,\\ 0 & \text{otherwise} .\end{cases} \tag{7}$$

Equations (6) and (7) will be useful in Sec. III for our sum-rule analysis of the free energies of TIM's.

Table I lists the MC results for the excess internal energy normalized by Nk_BT,

$$u_{\rm ex}^{\rm BIM}\equiv\sum_{i,j}\frac{Nx_ix_j}{2Vk_BT}\int d\mathbf{r}\frac{Z_iZ_je^2}{r}[g_{ij}(r)-1] , \tag{8}$$

together with the deviation

$$\Delta u_{\rm ex}^{\rm BIM}\equiv u_{\rm ex}^{\rm BIM}-u_{\rm LM} \tag{9}$$

from the linear mixing (LM) value

$$u_{\rm LM}\equiv\sum_i x_i u_{\rm ex}^{\rm OCP}(\Gamma_i) , \tag{10}$$

where we use [6]

$$u_{\rm ex}^{\rm OCP}(\Gamma)=-0.898\,004\Gamma+0.967\,86\Gamma^{0.25}+0.220\,703\Gamma^{-0.25}-0.860\,97 \tag{11}$$

for the excess internal energy of the OCP fluids. To calculate phase diagrams, we need to determine $u_{\rm ex}^{\rm BIM}$ with errors much smaller in magnitude than the values of the thermal energy; that is, with relative errors less than 0.1%. We see that the values of $u_{\rm ex}^{\rm BIM}$ given in Table I do have sufficient accuracy for this purpose.

The cases with $R_Z=\frac{4}{3}$ in Tables I and III include the MC runs performed and presented earlier in Refs. [10] and [22]. However, the values of $u_{\rm ex}^{\rm BIM}$ given in Tables I and III correct the values cited previously in Table I of Ref. [10]. The MC simulations, performed using periodic boundary conditions, collect the interaction energies between the different particles, as well as those between self-images that remain constant during the runs. In some of the old runs reported in Refs. [10] and [22], the terms between self-images were not correctly computed.

From Table I, we see that the LM formula, Eq. (10), reproduces $u_{\rm ex}^{\rm BIM}$ with relative errors less than 1% for all cases. We also find that the magnitude of $\Delta u_{\rm ex}^{\rm BIM}$ decreases proportionally to Γ_1^{-1}; that is, $|\Delta u_{\rm ex}^{\rm BIM}/u_{\rm ex}^{\rm BIM}|\propto\Gamma_1^{-2}$. This is connected with the behavior of the first-peak positions of $g_{ij}(r)$, which obey the IS scaling with increasing accuracy at larger Γ_1. It is remarkable—and very important for the phase diagrams—that $\Delta u_{\rm ex}^{\rm BIM}$ tends to take on negative values in the limit of $x\to 0$ for all values of R_Z. We have fitted the values of $\Delta u_{\rm ex}^{\rm BIM}$ in Table I with the formula

$$\Delta u_{\rm ex}^{\rm BIM}(R_Z,x,\Gamma_1)=0.32\frac{\sqrt{R_Z-1}(xR_Z-0.11)}{R_Z-0.22}\times\frac{x^{0.5}+2\times10^{-3}}{x^{1.7}+5\times10^{-5}}\frac{x(1-x)}{\Gamma_1} . \tag{12}$$

Figure 2 compares the MC values of $\Delta u_{\rm ex}^{\rm BIM}$ for $R_Z=3$ and 5 with this fitting formula, confirming the accuracy of the fit for both cases. In the figure, the MC values for $R_Z=3$ (5) are plotted by solid circles, open circles, and triangles, at $\Gamma_1=10$ (5), 15 (7), and 20 (10), respectively; the results given by Eq. (12) at the corresponding values

TABLE I. MC results for the normalized excess internal energy $u_{\rm ex}^{\rm BIM}$ for various BIM fluids. $\Delta u_{\rm ex}^{\rm BIM}$ is the deviation from the OCP LM value defined by Eqs. (9)–(11).

R_Z	x	Γ_1	$u_{\rm ex}^{\rm BIM}$	$\Delta_{\rm ex}^{\rm BIM}$
$\frac{4}{3}$	0.050 781	180.0	−163.938±0.003	−0.014
$\frac{4}{3}$	0.160 156	159.574	−154.712±0.003	−0.004
$\frac{4}{3}$	0.160 156	191.489	−186.042±0.003	0.007
$\frac{4}{3}$	0.420 898	200.0	−222.940±0.005	0.138
$\frac{4}{3}$	0.480 469	163.636	−187.534±0.005	−0.022
$\frac{4}{3}$	0.5	163.636	−189.259±0.006	0.010
$\frac{4}{3}$	0.5	200.0	−231.814±0.006	−0.032
3	0.01	10.0	−8.461±0.001	−0.004
3	0.05	10.0	−10.301±0.001	0.000
3	0.1	10.0	−12.602±0.001	0.004
3	0.2	10.0	−17.208±0.001	0.009
3	0.5	10.0	−31.035±0.002	0.013
3	0.01	15.0	−13.012±0.001	−0.003
3	0.05	15.0	−15.791±0.001	−0.001
3	0.1	15.0	−19.265±0.001	0.001
3	0.2	15.0	−26.212±0.001	0.007
3	0.5	15.0	−47.066±0.002	0.009
3	0.01	20.0	−17.602±0.001	−0.002
3	0.05	20.0	−21.319±0.001	−0.001
3	0.1	20.0	−25.963±0.001	0.004
3	0.2	20.0	−35.260±0.002	0.003
3	0.5	20.0	−63.145±0.002	0.008
5	0.01	5.0	−4.354±0.001	0.001
5	0.05	5.0	−6.741±0.001	0.007
5	0.1	5.0	−9.726±0.001	0.015
5	0.2	5.0	−15.702±0.001	0.023
5	0.5	5.0	−33.652±0.002	0.027
5	0.01	7.0	−6.279±0.001	0.000
5	0.05	7.0	−9.639±0.001	0.007
5	0.1	7.0	−13.842±0.001	0.013
5	0.2	7.0	−22.253±0.001	0.020
5	0.5	7.0	−47.504±0.002	0.022
5	0.01	10.0	−9.205±0.001	−0.002
5	0.05	10.0	−14.028±0.001	0.004
5	0.1	10.0	−20.057±0.001	0.011
5	0.2	10.0	−32.126±0.002	0.015
5	0.5	10.0	−68.343±0.003	0.015

of Γ_1 are drawn as solid, dashed, and dotted curves.

The excess free energy normalized by Nk_BT is calculated by integrating u_{ex}^{BIM}:

$$\Delta f_{ex}^{BIM}(R_Z,x,\Gamma_1)=\int_1^{\Gamma_1}\frac{d\Gamma_1'}{\Gamma_1'}\Delta u_{ex}^{BIM}(R_Z,x,\Gamma_1') +\Delta f_{ex}^{BIM}(R_Z,x,\Gamma_1=1)\ . \quad (13)$$

For $\Gamma_1 \lesssim 1$, the hypernetted-chain (HNC) scheme [23] gives the free energy for the fluid mixture with reliable accuracy. To obtain the integration constant in Eq. (13), we have thus solved the HNC equations at $\Gamma_1=1$ for BIM's with $R_Z=\{2,3,4,5\}$ and $x=\{0.01,0.1,0.2,0.3,0.5,0.7\}$, and we have fitted the results with the formula

$$\Delta f_{ex}^{BIM}(R_Z,x,\Gamma_1=1)=\frac{0.0551(R_Z-1)^{1.8}x(1-x)}{1+1.12(R_Z-1)x} \quad \text{for } R_Z\le 5\ . \quad (14)$$

This expression fits the tabular data with errors less than 0.001. Taking the charge-neutrality requirement for the mixture into account, and recalling that by hypothesis the electron density is independent of the concentrations x_i in a BIM, we find [9] that the ideal part of the free energy is given by

$$\Delta f_{id}=\sum_i x_i \ln\left[\frac{x_iZ_i}{\sum_j x_jZ_j}\right]\ . \quad (15)$$

The Helmholtz free energy normalized by Nk_BT for BIM fluids with $R_Z\le 5$ is therefore expressed as [20]

$$\Delta f^{BIM}(R_Z,x,\Gamma_1)\equiv\Delta f_{ex}^{BIM}+\Delta f_{id}$$

$$=0.32\frac{\sqrt{R_Z-1}(xR_Z-0.11)}{R_Z-0.22}\frac{(x^{0.5}+2\times10^{-3})}{(x^{1.7}+5\times10^{-5})}x(1-x)\left[1-\frac{1}{\Gamma_1}\right] +\frac{0.0551(R_Z-1)^{1.8}x(1-x)}{1+1.12(R_Z-1)x}+(1-x)\ln\left[\frac{1-x}{1-x+xR_Z}\right]+x\ln\left[\frac{xR_Z}{1-x+xR_Z}\right], \quad (16)$$

which we shall use for the analysis of the phase diagrams.

The finding that $\Delta u_{ex}^{BIM}<0$, and consequently that $[\Delta f_{ex}^{BIM}(R_Z,x,\Gamma)-\Delta f_{ex}^{BIM}(R_Z,x,\Gamma=1)]<0$, for $x\ll 1$ ($\Gamma>1$) is confirmed independently by the following sum-rule analysis arising from the requirement of thermodynamic consistency. It has been shown [20,24,25] that the OCP screening potential at the origin equals the difference in the excess free energies before and after a nuclear-fusion reaction between two (identical) ions:

$$\frac{H(0)}{k_BT}=2f_{ex}^{OCP}(\Gamma)-f_{ex}^{OCP}(2^{5/3}\Gamma) -\left[\frac{\partial}{\partial x}\Delta f_{ex}^{BIM}(R_Z=2,x,\Gamma_1=\Gamma)\right]_{x\to 0}\ . \quad (17)$$

The term involving the partial derivative of Δf_{ex}^{BIM} arises from the fact that the excess free energy *after* the reaction is that of a BIM with a single nucleus of charge $2Ze$ embedded in an OCP consisting of ions of charge Ze. We calculate the OCP excess free energy from [6]

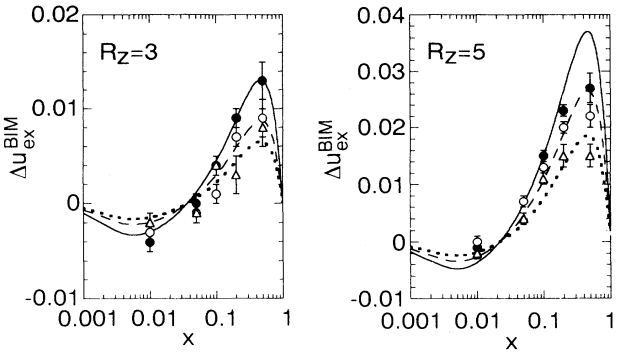

FIG. 2. The normalized excess internal energies for BIM fluids with $R_Z=3$ and 5. The MC values for $R_Z=3$ (5) are plotted by solid circles, open circles, and triangles at $\Gamma_1=10$ (5), 15 (7), and 20 (10), respectively; the solid, dashed, and dotted curves represent Eq. (12) at the corresponding values of Γ_1.

$$f_{ex}^{OCP}(\Gamma)=-0.898\,004\Gamma+3.871\,44\Gamma^{0.25} -0.882\,812\Gamma^{-0.25}-0.860\,97\ln\Gamma -2.526\,92\ . \quad (18)$$

The screening potential $H(0)$ is given by Eq. (6), with $Z_i=Z_j$ and $a_i=a_j$. For $\Gamma=100$ (40), we find that the left-hand side of Eq. (17) assumes the values $H(0)/k_BT=110.099$ (44.437). From Eq. (18), we obtain the corresponding values $2f_{ex}^{OCP}(\Gamma)-f_{ex}^{OCP}(2^{5/3}\Gamma)=107.795$ (43.528), and from the expression given in Eq. (16), the right-hand side of Eq. (17) takes on the values 110.011 (45.709). Thus the derivative of Δf_{ex}^{BIM} at $x\to 0$ has the correct sign to ensure the sum-rule requirement Eq. (17).

The physical reason for the result $\Delta u_{ex}^{BIM}<0$ at $x\ll 1$ in a BIM *fluid* may be traced to the failure of a thermodynamic description based on the IS model when it is applied to an extreme case in which one of the ionic constituents is dilute and thus is inherently in the weak-coupling

regime. We recall that Eq. (11), on which the LM formula is based, applies only to a plasma in strong coupling and that for $\Gamma < 1$ (i.e., weak coupling) it gives a result that is *smaller* in magnitude than that which one would calculate from the Debye-Hückel or Abe formulas [26], for instance. The true MC values for the excess internal energy are therefore larger in magnitude than the LM calculation based on the strong-coupling formula. For a BIM *solid,* however, an IS model provides a relatively accurate result irrespective of the value of x; hence $\Delta u_{\rm ex}^{\rm BIM} > 0$ in a BIM solid even with $x \ll 1$, as we shall find in Sec. III B.

B. Solid phase

It is well known that the OCP in its ground state assumes a bcc lattice structure. This conclusion is obtained through comparison of the Madelung energies [27] of the several cubic lattice structures and that of the hexagonal-close-packed (hcp) lattice. Extensive MC simulations have been performed for OCP solids with cubic structures [5,6,28–30], and the bcc lattice has been shown to have the lowest free energy at finite temperatures as well.

The free energies of solid mixtures, containing ions with differing charges, depend on the specific ionic configurations. We have little knowledge of these structure for BIM solids under equilibrated conditions. Outstanding issues include the following questions: Do BIM's form "disordered" solids instead of regular, crystalline solids? How does the equilibrium structure depend on the temperature or density? To elucidate these issues, we first calculate BIM Madelung energies for both crystalline and disordered solids. The excess internal energies at finite temperatures for each type of solid are then evaluated by the MC simulation method. Combining these results, we estimate the free energies and thus determine the equilibrated structures for the BIM solids.

The OCP Madelung energy is $E_M^{\rm OCP}/[N(Ze)^2/a] = -0.895\,929$ for the bcc structure, lower than either the value $-0.895\,874$ for the face-centered-cubic (fcc) structure or the value $-0.895\,838$ for the hcp structure [27]. It is thus reasonable to assume that BIM's with $R_Z \approx 1$ have the lowest energies when all the ions form a bcc structure. We have therefore computed Madelung energies $E_M^{\rm BIM}$ for each of the following three types of BIM *metastable* solids, each of which has an underlying bcc structure: (1) a "random solid," appropriate for any value of x, which is obtained by randomly distributing all of the particles on bcc lattice sites and then moving particles in the directions of the force acting on them; (2) a "CsCl-type crystal," which corresponds to an underlying bcc structure with $x = 0.5$, where the two species of particles each form interpenetrating simple cubic lattices [27,31]; and (3) a "4{fcc}-type crystal," for $x = 0.25$ and 0.75, where the bcc sites are divided into four equivalent fcc sites, and each of the four is occupied by particles of the same species.

The Madelung energies for random solids have been calculated for 20 different combinations of $R_Z = \{\frac{4}{3}, \frac{5}{3}, 2, 3, 4\}$ and $x = \{\frac{5}{432}, 0.25, 0.5, 0.75\}$ using $N = 432$ particles. Starting from a random-bcc configuration, where all the particles are distributed randomly on the bcc sites, we look for local minima in the energy by displacing particles along the force directions computed from all the surrounding particles following the conjugate-gradient procedure [32]. We define the Madelung energy $E_M^{\rm BIM}$ for a random solid as the average of the interaction energies obtained from several different random simulations, each with a different starting configuration, which we shall call "starts" for brevity.

For the CsCl- and 4{fcc}-type crystals, we have examined the stability of the crystals by displacing all the particles from the initial lattice sites in random directions by an amount $\delta r = 0.05(4\pi N/3V)^{-1/3}$. We have thus confirmed that these crystalline configurations are stable for $R_Z \leq 4$.

Table II lists the Madelung energies for random solids

TABLE II. The deviation of the normalized Madelung energy from the OCP LM value for various BIM solids defined by Eq. (19). See text for the explanation of "Type of start."

R_Z	x	Type of start	$\Delta E_M^{\rm BIM}/N(Z_1e)^2/a_1$
$\frac{4}{3}$	0.011 57	random bcc	0.000 07±0.000 01
$\frac{4}{3}$	0.25	random bcc	0.000 93±0.000 02
$\frac{4}{3}$	0.25	4{fcc}	0.000 75
$\frac{4}{3}$	0.5	random bcc	0.001 26±0.000 02
$\frac{4}{3}$	0.5	CsCl	−0.000 06
$\frac{4}{3}$	0.75	random bcc	0.000 97±0.000 02
$\frac{4}{3}$	0.75	4{fcc}	0.001 03
$\frac{5}{3}$	0.011 57	random bcc	0.000 20±0.000 01
$\frac{5}{3}$	0.25	random bcc	0.003 00±0.000 05
$\frac{5}{3}$	0.25	4{fcc}	0.002 42
$\frac{5}{3}$	0.5	random bcc	0.004 00±0.000 04
$\frac{5}{3}$	0.5	CsCl	−0.000 19
$\frac{5}{3}$	0.75	random bcc	0.003 60±0.000 06
$\frac{5}{3}$	0.75	4{fcc}	0.004 26
2	0.011 57	random bcc	0.000 41±0.000 01
2	0.25	random bcc	0.003 65±0.000 04
2	0.25	4{fcc}	0.004 53
2	0.5	random bcc	0.005 03±0.000 05
2	0.5	CsCl	−0.000 24
2	0.75	random bcc	0.0065±0.0001
2	0.75	4{fcc}	0.009 84
3	0.011 57	random bcc	0.001 13±0.000 02
3	0.25	random bcc	0.003 61±0.000 06
3	0.25	4{fcc}	0.011 34
3	0.5	random bcc	0.006 24±0.000 07
3	0.5	CsCl	0.001 34
3	0.75	random bcc	0.011 7±0.0001
3	0.75	4{fcc}	0.040 59
4	0.011 57	random bcc	0.001 65±0.000 02
4	0.25	random bcc	0.002 88±0.000 06
4	0.25	4{fcc}	0.017 21
4	0.5	random bcc	0.0073±0.0001
4	0.5	CsCl	0.006 78
4	0.75	random bcc	0.0169±0.0002
4	0.75	4{fcc}	0.091 17

obtained from ten starts, as well as for the CsCl- and 4{fcc}-type crystals, in the form of deviations from a LM calculation based on the OCP values:

$$\frac{\Delta E_M^{\rm BIM}}{N(Z_1e)^2/a_1} \equiv \frac{E_M^{\rm BIM}}{N(Z_1e)^2/a_1} + 0.895\,929(1-x+xR_Z^{5/3}) . \quad (19)$$

In the cases of lattice simulations, no error assessment is involved because of the accuracy. It is remarkable that CsCl-type crystals at $x=0.5$ for $R_Z \le 4$ and 4{fcc}-type crystals at $x=0.25$ for $R_Z \le \frac{5}{3}$ have significantly lower energies $\Delta E_M^{\rm BIM}$ than do the random solids. We note that $\Delta E_M^{\rm BIM}$ for a CsCl-type crystal becomes negative for $R_Z \lesssim 2.3$. The high degree of symmetry of these special types of crystal structures evidently permits a substantial reduction in the energy (cf. Ref. [27]).

The Madelung energies computed for the *random* solids are plotted in Fig. 3 as crosses ($R_Z=\frac{4}{3}$), triangles ($R_Z=\frac{5}{3}$), squares ($R_Z=2$), open circles ($R_Z=3$), and solid circles ($R_Z=4$), to illustrate their dependences on R_Z and x. For $R_Z \le \frac{4}{3}$, we find that the values of $\Delta E_M^{\rm BIM}$ for the random solids are symmetric with respect to inversion of x. As R_Z increases, the peak in $\Delta E_M^{\rm BIM}$ begins to shift toward $x=1$, and the peak height increases. In contrast to our finding that $\Delta u_{\rm ex}^{\rm BIM} < 0$ for $x \ll 1$ for the BIM fluid phases, the Madelung-energy deviations $\Delta E_M^{\rm BIM}$ remain positive even for $x \ll 1$. An analytic approximation for $\Delta E_M^{\rm BIM}$ for the random solids with $R_Z \lesssim 4.5$ is

$$\frac{\Delta E_M^{\rm BIM}}{N(Z_1e)^2/a_1} = \frac{\dfrac{0.05(R_Z-1)^2x(1-x)}{[1+0.64(R_Z-1)][1+0.5(R_Z-1)^2]}}{1+\dfrac{27(R_Z-1)}{1+0.1(R_Z-1)}\sqrt{x}\,(\sqrt{x}-0.3)(\sqrt{x}-0.7)(\sqrt{x}-1)} . \quad (20)$$

This expression is plotted in Fig. 3 as dotted ($R_Z=\frac{4}{3}$), dashed ($R_Z=\frac{5}{3}$), long-dashed ($R_Z=2$), dot-dashed ($R_Z=3$), and solid ($R_Z=3$) curves.

The reason why the peak in $\Delta E_M^{\rm BIM}$ for a random solid shifts from $x=0.5$ toward $x=1$ as R_Z increases may be explained as follows. Particles "2" (larger Z) make larger contributions to the interaction energy than do particles "1." Thus the particles "2" as "contaminants" in a lattice of particles "1" act to destroy the crystalline order more efficiently than do particles "1" as contaminants in a crystal of particles "2." This can be seen directly by examining the microscopic particle configurations. In this way, we find that crystalline order is destroyed for BIM's with $R_Z \gtrsim \frac{5}{3}$ at $x=0.25$ and for BIM's with $R_Z \gtrsim 3$ at $x=0.75$; that is, there are different threshold values of R_Z below which regular crystalline order exists. Figure 4 shows examples of projection maps of particles in BIM's with $R_Z=2$ at $x=0.25$ and 0.75, where the crosses and circles represent particles of species "1" and "2," respectively. For $x=0.75$, we clearly observe a crystalline order of the particles, while the particles are disordered for $x=0.25$. The destruction of crystalline order can also be demonstrated quantitatively by an examination of the first-peak position $r_{{\rm pk},ij}$ of $g_{ij}(r)$. We find [33] that the deviation from the IS-scaling value, $\xi_{ij} \equiv r_{{\rm pk},ij}/a_{ij} - 1.76$ with $a_{ij} \equiv (a_i+a_j)/2$, is larger in magnitude for $(i,j)=(1,1)$ than for either the (1,2) or the (2,2) pairs, and that, in addition, $|\xi_{11}|$ grows in proportion to $x^{1.3}$. The

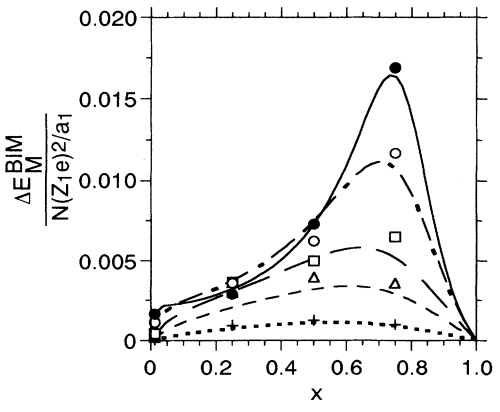

FIG. 3. The normalized Madelung energies for BIM random solids. Numerical results are plotted by crosses ($R_Z=\frac{4}{3}$), triangles ($R_Z=\frac{5}{3}$), squares ($R_z=2$), open circles ($R_Z=3$), and solid circles ($R_Z=5$); the dotted, dashed, long-dashed, dot-dashed, and solid curves represent the results given by Eq. (20) at the corresponding values of R_Z.

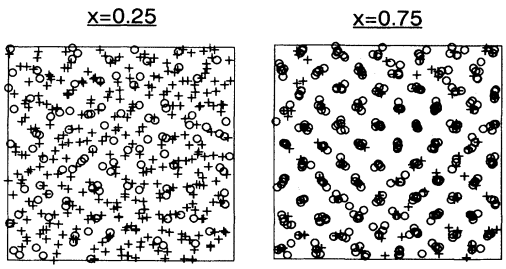

FIG. 4. Projection maps of particles in the ground state for random solids with $R_Z=2$ and with $x=0.25$ (left) and 0.75 (right). Both maps represent projections onto the ⟨100⟩ direction of the initial bcc lattice. In each panel, the crosses and circles represent particles of species "1" and "2," respectively.

destruction of crystalline order observed for $x<0.5$ reduces the deviation in $r_{\mathrm{pk},ij}$ from the IS scaling, and hence acts to lower the Madelung energy toward the LM value.

The internal structure of a BIM solid in the ground state, as given by the present $\Delta E_M^{\mathrm{BIM}}$ analysis, is either one that is phase separated into a CsCl-type crystal together with a pure crystal of species "1" or "2" (for $R_Z \lesssim 2.3$), or else it is one that is phase separated into pure crystals of each species (for $R_Z > 2.3$). These predictions apply only at temperatures far below the melting temperature, however, as we show by the following calculation of the internal energies at finite temperatures from our MC simulations.

Starting from random, CsCl-type, or 4{fcc}-type distributions on bcc sites, we have performed MC simulations for BIM solids with $R_Z=\{\frac{4}{3},\frac{5}{3},2,3,4\}$, at various values of x and Γ_1, using $N=1024$ particles. In addition, MC runs for random fcc starts have been performed for $R_Z=3$ and $x=\frac{9}{864}$, using $N=864$ particles. In averaging the energy over the initial distributions for the random bcc and fcc solids with $R_Z=\frac{4}{3}$, we have incorporated particle-exchange trials [10] in the Metropolis algorithm in addition to the usual displacement trials. For $R_Z \geq \frac{5}{3}$, the internal energies are averaged over five separate MC runs.

We found that the system did not reach thermal equilibrium even after 5×10^6 configurations for random bcc starts with $R_Z \geq \frac{5}{3}$ and $x>0.1$; a similar failure to equilibrate occurred for the 4{fcc}-type starts with $R_Z \geq 2$ and $x=0.25$ and 0.75. In other cases, an equilibrium was reached after $(1-3)\times10^6$ configurations. Table III lists the excess internal energy $u_{\mathrm{ex}}^{\mathrm{BIM}}$, together with the deviation $\Delta u_{\mathrm{ex}}^{\mathrm{BIM}}$ from the LM values, defined in Eq. (9), where we have used

$$u_{\mathrm{ex}}^{\mathrm{OCP}}(\Gamma)=-0.895\,929\Gamma+1.5+\frac{10.84}{\Gamma}+\frac{352.8}{\Gamma^2}+\frac{1.74\times10^5}{\Gamma^3} \tag{21}$$

as the excess internal energy [7] for the OCP solids. It is remarkable that the values of $\Delta u_{\mathrm{ex}}^{\mathrm{BIM}}$ for the BIM solids are *directly* proportional to Γ_1, in contrast to the behavior of the BIM fluids, where $\Delta u_{\mathrm{ex}}^{\mathrm{BIM}} \propto \Gamma_1^{-1}$. The reason for this is that the Madelung energy, which is proportional to Γ_1, is the principal term in $u_{\mathrm{ex}}^{\mathrm{BIM}}$ for the solids. We note in passing that no substantial difference in $\Delta u_{\mathrm{ex}}^{\mathrm{BIM}}$ could be seen between random bcc and random fcc starts at $R_Z=3$ and $x\approx0.01$.

Table III compares the quantities $\Delta u_{\mathrm{ex}}^{\mathrm{BIM}}$ with the Madelung energies for the corresponding R_Z, x, and types of start. To evaluate $\Delta E_M^{\mathrm{BIM}}$, we have used Eq. (20) for the cases with $x=0.050\,78$, $0.160\,16$, $0.610\,35$, and $0.770\,51$; for other cases, the values in Table II have been adopted. We find that the results for $\Delta u_{\mathrm{ex}}^{\mathrm{BIM}}$ at finite temperatures are all reproduced with good accuracy by the Madelung energies:

$$\Delta u_{\mathrm{ex}}^{\mathrm{BIM}} \simeq \frac{\Delta E_M^{\mathrm{BIM}}}{Nk_BT}\ . \tag{22}$$

As far as random solids are concerned, the possible errors in $\Delta u_{\mathrm{ex}}^{\mathrm{BIM}}$ calculated from Eqs. (20) and (22) are ±0.02 at most.

Since $\Delta E_M^{\mathrm{BIM}}/(Nk_BT)$ is proportional to Γ_1, the excess free energy for a BIM solid is thus

TABLE III. MC results for the normalized excess internal energy $u_{\mathrm{ex}}^{\mathrm{BIM}}$ for various BIM solids. The quantity $\Delta u_{\mathrm{ex}}^{\mathrm{BIM}}$ is the deviation from the OCP LM value defined by Eqs. (9) and (21), to be compared with the corresponding Madelung energy $\Delta E_M^{\mathrm{BIM}}$. See text for the explanation of "Type of start."

R_Z	x	Γ_1	Type of start	$u_{\mathrm{ex}}^{\mathrm{BIM}}$	$\Delta u_{\mathrm{ex}}^{\mathrm{BIM}}$	$\Delta E_{\mathrm{M}}^{\mathrm{BIM}}/(Nk_BT)$
$\frac{4}{3}$	0.050 78	180.0	random bcc	-164.675 ± 0.003	0.031	0.040
$\frac{4}{3}$	0.050 78	360.0	random bcc	-330.994 ± 0.003	0.081	0.080
$\frac{4}{3}$	0.160 16	191.469	random bcc	-186.768 ± 0.003	0.093	0.105
$\frac{4}{3}$	0.160 16	382.979	random bcc	-375.213 ± 0.003	0.186	0.210
$\frac{4}{3}$	0.5	163.636	random bcc	-189.949 ± 0.005	0.167	0.178
$\frac{4}{3}$	0.5	200.0	random bcc	-232.542 ± 0.004	0.199	0.218
$\frac{4}{3}$	0.5	200.0	CsCl	-232.765 ± 0.003	-0.024	-0.012
$\frac{4}{3}$	0.5	360.0	random bcc	-419.839 ± 0.004	0.381	0.392
$\frac{4}{3}$	0.610 35	163.636	random bcc	-199.920 ± 0.004	0.156	0.179
$\frac{4}{3}$	0.770 51	200.0	random bcc	-262.414 ± 0.004	0.159	0.170
$\frac{5}{3}$	0.25	200.0	4{fcc}	-237.268 ± 0.003	0.503	0.484
$\frac{5}{3}$	0.5	200.0	CsCl	-297.991 ± 0.004	-0.050	-0.038
$\frac{5}{3}$	0.75	200.0	4{fcc}	-357.259 ± 0.004	0.853	0.852
2	0.5	200.0	CsCl	-372.553 ± 0.004	-0.072	-0.048
3	0.010 74	250.0	random bcc	-234.75 ± 0.02	0.28	0.28
3	0.010 42	250.0	random fcc	-234.35 ± 0.01	0.29	
3	0.5	200.0	CsCl	-646.893 ± 0.004	0.235	0.268
4	0.5	200.0	CsCl	-989.841 ± 0.004	1.246	1.356

$$\Delta f_{\rm ex}^{\rm BIM}=\frac{\Delta E_M^{\rm BIM}}{Nk_BT} . \tag{23}$$

We here propose that the total Helmholtz free energy of the BIM solid is given by

$$\Delta f^{\rm BIM}=\frac{\Delta E_M^{\rm BIM}}{Nk_BT}-\frac{\Delta S^{\rm BIM}}{Nk_B} , \tag{24}$$

where the entropy of mixing $\Delta S^{\rm BIM}$ is calculated by counting the number of different configurations; that is,

$$\frac{\Delta S^{\rm BIM}}{Nk_B}=\begin{cases}0 & \text{for crystalline solids}\\ -\Delta f_{\rm id}(R_Z,x) & \text{for random solids.}\end{cases} \tag{25}$$

We remark that the R_Z dependence of $\Delta S^{\rm BIM}$ for random solids is one of the essential elements of an ionic mixture; it is responsible for the distortion or destruction of the lattice order in a random solid, as depicted in Fig. 4.

From the free energies thus calculated for the three different types of solids used in our MC simulations, we can now determine the equilibrated structures for the BIM solids. As noted above, we find that, *in the ground state,* BIM's form CsCl-type crystals for $R_Z\le 2.3$ and mixtures of pure crystals of each species for $2.3<R_Z\le 5$. At finite temperatures, however, the entropy-of-mixing term becomes substantial and the equilibrium structure may change. Comparison of the values of $\Delta f^{\rm BIM}$ for the random and CsCl-type solids at $x=0.5$ shows that the *random* solid has the lower free energy for Γ_1 smaller than 600 ($R_Z=\frac{4}{3}$), 210 ($R_Z=\frac{5}{3}$), 150 ($R_Z=2$), 140 ($R_Z=3$), and 2000 ($R_Z=4$). These Γ_1 values are in fact much larger than those at solidification, as estimated from $\Gamma_{\rm eff}\equiv(1-x)\Gamma_1+x\Gamma_2=(1-x+xR_Z^{5/3})\Gamma_1\sim 180$. In the construction of phase diagrams in Sec. II C, we thus use the formulas for random solids in Eq. (25) to calculate the free energies for BIM solids.

C. Phase diagrams

We first calculate phase diagrams for the BIM's under the condition of rigid uniform background charges, using the Helmholtz free energies for both fluid and solid phases obtained in Sec. II B. For application to the interiors of WD's, we then extend the calculations to construct phase diagrams at constant pressure, including the compressibility of the relativistically degenerate electrons.

Phase diagrams for BIM's are determined by comparing the Helmholtz free energies

$$f^{\rm BIM}=(1-x)f^{\rm OCP}(\Gamma_1)+xf^{\rm OCP}(\Gamma_2)+\Delta f^{\rm BIM} \tag{26}$$

for the fluids and the random solids. Here we use

$$\begin{aligned}f^{\rm OCP}(\Gamma)=&-0.898\,004\Gamma+3.871\,44\Gamma^{0.25}\\&-0.882\,812\Gamma^{-0.25}\\&+2.139\,03\ln\Gamma-3.242\,22\end{aligned} \tag{27}$$

as the free energy for the OCP fluid [6], and

$$f^{\rm OCP}(\Gamma)=-0.895\,929\Gamma+\tfrac{9}{2}\ln\Gamma-1.885\,596-\frac{10.84}{\Gamma}-\frac{176.4}{\Gamma^2}-\frac{5.980\times 10^4}{\Gamma^3} , \tag{28}$$

for the OCP solid [7]. In cases where it is necessary to extrapolate Eq. (28) to values of $\Gamma\le 100$, we set the last three terms, representing the anharmonicity in the thermal motions of particles, to the values at $\Gamma=100$, in order to preserve the requirement that $f^{\rm OCP}$(solid) $>f^{\rm OCP}$(fluid) for $\Gamma<100$.

Examples of the phase diagrams thus constructed are shown in Figs. 5(a)–5(d) for BIM's with $R_Z=\frac{4}{3}$, $\frac{3}{2}$, $\frac{5}{3}$, and $\frac{13}{3}$, respectively; the quantity T_m is the freezing temperature given by Eq. (1) for an OCP of "1" particles. By specific calculations, we find that demixing into two different fluid phases does *not* occur at *any* temperature for $R_Z\le 4.5$, as we show explicitly at the end of this subsection. The R_Z dependence of the phase diagrams can be summarized as follows: For BIM's with $R_Z\lesssim 1.4$, the diagrams are of the azeotropic type, and no chemical separation occurs at solidification *except* for $x<0.01$. Phase diagrams for $R_Z\approx 1.5$ have composite structures, containing features of both the azeotropic and the eutectic diagrams: for $x>0.4$, a "2"-rich solid with $x=0.8$–0.9 is produced at solidification, while a mixed solid emerges from the fluid for $x<0.4$. For $R_Z\gtrsim 1.6$, the phase diagrams are of the eutectic type, and nearly pure solids of species "1" and "2" form at solidification.

Chemical separation takes place upon solidification when $\Delta f^{\rm BIM}=\Delta f_{\rm ex}^{\rm BIM}-\Delta S^{\rm BIM}/(Nk_B)>0$ holds for all x in the solid phase, a condition that is actually satisfied when $R_Z\gtrsim 1.6$. The sharp decrease in the freezing temperature when $x\ll 1$ in the azeotropic phase diagrams [cf. Fig. 5(a)] is a consequence of the finding that $\Delta f_{\rm ex}^{\rm BIM}<0$ when $x\ll 1$ in the BIM fluids [cf. Eq. (16)].

Ichimaru, Iyetomi, and Ogata [10] originally predicted an azeotropic phase diagram for a BIM with $R_Z=\frac{4}{3}$. For the fluid phase, they set $\Delta f_{\rm ex}^{\rm BIM}=0$, based on MC simulations performed at $x=0.4$–0.5 and on integral-equation results, and they evaluated $\Delta f^{\rm BIM}$ variationally for the solid by a density-functional method. The azeotropic diagram in Ref. 10 results from the lower value of $\Delta f^{\rm BIM}$ for the solid compared to that of the fluid [22,34]. In the present work, we have improved the free-energy formula for BIM fluids by performing accurate MC simulations for various R_Z and x and by exploiting a sum rule for the excess free energy. For the solid phase, we have also improved the free-energy formula by analyses of the Madelung energies and of the internal energies at finite temperatures, as computed from the MC simulations.

It has been pointed out [35] that the oscillatory behavior of the normalized radial distribution function for strongly coupled OCP's resembles that for the hard-sphere (HS) system, even though the interaction range for a HS system is limited to lie within the HS diameter, while it is infinite for the OCP. For that reason, it is interesting to compare the present phase diagrams for BIM's with those for HS mixtures. Barrat, Baus, and Hansen [36] evaluated the free energy for HS mixtures

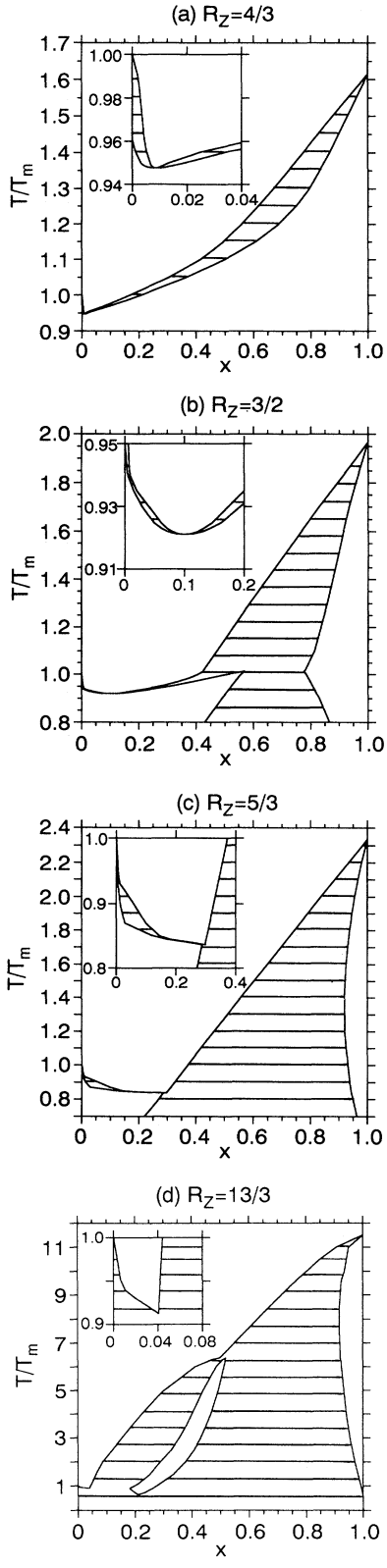

FIG. 5. Phase diagrams for BIM's with constant, uniform background-charge density: $R_Z=$ (a) $\frac{4}{3}$, (b) $\frac{3}{2}$, (c) $\frac{5}{3}$, and (d) $\frac{13}{3}$. The scaling parameter T_m is the freezing temperature for a 1-OCP.

with diameter ratios α both for the fluid and the solid phases using a density-functional method, and they constructed the corresponding phase diagrams. The diagrams they obtained for the HS mixtures have a spindle-type structure for $\alpha=1-1.06$, an azeotropic structure for $\alpha=1.06-1.09$, and a eutectic structure for $\alpha>1.09$. In addition, they found nearly complete immiscibility for $\alpha>1.18$. According to the ion-sphere model for a BIM, the charge ratio R_Z may be tentatively interpreted as $\alpha=R_Z^{1/3}$. The characteristic charge ratio, $R_Z=1.5$, at which the BIM phase diagrams change from azeotropic to eutectic, would thus correspond to $\alpha=1.5^{1/3}=1.14$. Despite the differences between the HS and BIM interaction potentials, we thus find a reasonable correspondence between the phase diagrams of the two types of systems.

In actual applications to real, physical cases, including the interiors of WD's, phase diagrams constructed at constant pressures are more useful than those obtained by assuming the background charge distribution to be uniform. Such phase diagrams are based on the Gibbs free energies, rather than the Helmholtz free energies of the fluid and solid phases. For the mass densities $\rho_8\equiv 10^{-8}[\rho\ (\mathrm{g/cm^3})]\sim 10^{-1}-10^{2}$, and temperatures $T_6\equiv 10^{-6}[T\ (\mathrm{K})]\sim 1-10^{2}$ found in WD's, the electrons can be treated as being in the ground state, since the ratio of the thermal energy to the electron Fermi energy,

$$\frac{k_B T}{\varepsilon_F}=1.688\times 10^{-4} T_6[\sqrt{1+21.94(\rho_8/\mu_e)^{2/3}}-1]^{-1}\ , \tag{29}$$

is quite small. Here we measure the number density of electrons by the ratio [1]

$$r_s=\left[\frac{3}{4\pi n_e}\right]^{1/3}\frac{1}{a_B}=2.991\times 10^{-3}\left[\frac{\rho_8}{\mu_e}\right]^{-1/3}\ , \tag{30}$$

where $a_B=\hbar^2/me^2$ is the Bohr radius, and $\mu_e=\sum_i x_i A_i/\sum_i x_i Z_i$ is the mean molecular weight per electron. The Coulomb coupling parameters in Eq. (2) can be usefully rewritten in the form

$$\Gamma_i=105.5\frac{Z_i^{5/3}}{T_6}\left[\frac{\rho_8}{\mu_e}\right]^{1/3}\ . \tag{31}$$

The dominant contribution to the pressure in a WD comes from the relativistically degenerate electrons. Therefore, we treat the partial pressures coming from the ions as perturbations in comparison with the electron pressure. The Helmholtz free energy is

$$F=F_0+F_1\ , \tag{32}$$

where F_0 is the kinetic energy of the electrons,

$$F_0(V)=E_k^{\mathrm{el}}(r_s)\ , \tag{33}$$

and the quantity F_1 is the exchange energy [37,38] for the electrons plus the free energy for the ions:

$$F_1(V,T)=E_x^{\mathrm{el}}(r_s)+F^{\mathrm{ion}}(r_s,T)\ . \tag{34}$$

Up to the second order in F_1 the Gibbs free energy at a

pressure P and temperature T is given by

$$G(P,T)=F_0(V_0)+PV_0+F_1(V_0) -\frac{1}{2}\left[\frac{\partial F_1}{\partial V_0}\right]^2\left[\frac{\partial^2 F_0}{\partial V_0^2}\right]^{-1}. \quad (35)$$

Here the volume V_0 is determined by the condition

$$P=\left[-\frac{\partial F_0}{\partial V}\right]_{V=V_0}, \quad (36)$$

which can be conveniently written in the form

$$P=1.801\times10^{23}\ \text{dyn cm}^{-2}\left[y\sqrt{1+y^2}\left(\frac{2y^2}{3}-1\right) +\ln\left[y+\sqrt{1+y^2}\right]\right]. \quad (37)$$

Here we define $y\equiv0.014\,00/(r_s)_{V_0}$, where $(r_s)_{V_0}$ is the value of the parameter r_s [cf. Eq. (30)] when $V=V_0$.

We may examine the validity of the present perturbation treatment by calculating the variation of the volume, $\delta V=V-V_0$, as a function of x; that is,

$$\frac{\delta V}{V_0}=-\frac{1}{V_0}\frac{\partial F_1}{\partial V_0}\left[\frac{\partial^2 F_0}{\partial V_0^2}\right]^{-1}. \quad (38)$$

Setting $Z_1=6$, for instance, we find $|\delta V/V_0|\lesssim0.05$ for all x with $(r_s)_{V_0}\leq0.02$ and $R_Z\leq4.5$. We thus regard Eq. (35) as having sufficient accuracy to permit the determination of the phase diagrams in WD interiors.

Before considering the phase diagrams based on Eq. (35), we explore the possibility of phase separation [9] into two fluids having different compositions, x. In Fig. 6, the conditions for such a demixing are shown for dense C-O ($R_Z=\frac{4}{3}$), C-Ne ($R_Z=\frac{5}{3}$), and C-Fe ($R_Z=\frac{13}{3}$) fluids at $P=10^{22}$ dyn cm^{-2}, corresponding to $(r_s)_{V_0}=0.021\,45$. We find that the critical temperature T_c for demixing increases with R_Z, concurrent with a decrease in the critical concentration x_c. Specifically, we find $(T_c/(10^6\ \text{K}),x_c)=(0.027,0.38)$ for the C-O fluid, (0.11,0.31) for C-Ne, and (3.5,0.082) for C-Fe. Since the values of T_c for the C-O and C-Ne fluids are far below the freezing temperature, $T_m^C=1.7\times10^6$ K for a pure carbon OCP, solidification takes place prior to demixing for those fluids. For C-Fe fluids, however, T_c is comparable to T_m^C, leaving open for the moment the possibility that demixing may occur prior to solidification of this fluid. We will return to this issue below.

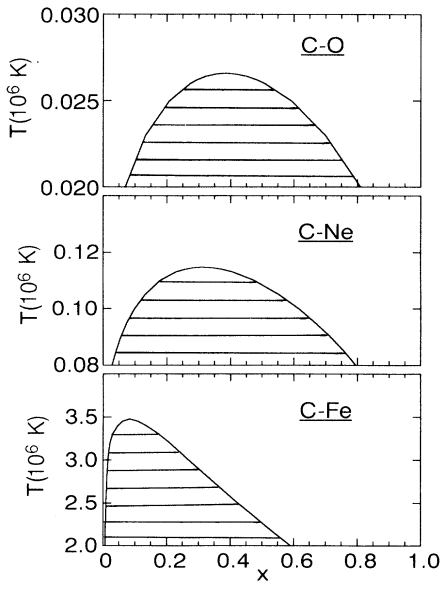

FIG. 6. Demixing curves for C-O, C-Ne, and C-Fe BIM fluids at $P=10^{22}$ dyn cm^{-2}.

We now resume our discussion of the phase diagrams for fluid-solid mixtures at constant pressure. Figures 7(a)–7(e) show the phase diagrams for dense O-Ne ($R_Z=\frac{5}{4}$), C-O ($R_Z=\frac{4}{3}$), O-Mg ($R_Z=\frac{3}{2}$), C-Ne ($R_Z=\frac{5}{3}$), and C-Fe ($R_Z=\frac{13}{3}$) matter at $P=10^{22}$ dyn cm^{-2}. The compressibility of the electrons changes the diagrams only slightly for $R_Z\lesssim\frac{5}{3}$; e.g., the eutectic concentration and temperature decrease only by 8% and 5%, respectively, for C–Ne matter in Fig. 7(c). For C-Fe matter, however, the eutectic concentration changes rather significantly from $x=0.04$ to $x=0.004$, as shown in Fig. 7(e). The fluid demixing curve for C-Fe matter, determined above, is superimposed in Fig. 7(e), where it is shown as a dotted curve. Thus we can finally resolve the question of whether or not demixing occurs prior to solidification: we find that demixing actually does *not* take place, even for a large-R_Z BIM such as C-Fe.

III. DENSE TERNARY-IONIC MIXTURES

In Sec. II, we presented phase diagrams for various BIM's and predicted chemical separation for BIM's with $R_Z\gtrsim1.6$. However, the dense matter in a WD sometimes must be represented more accurately, e.g., by a TIM rather than by a BIM. The chemical separation of such a mixture can significantly extend the final stages of stellar evolution. In many WD's, the matter in the interior may be well approximated [3,13,14] as a ^{12}C-^{16}O-^{22}Ne TIM, with $x_{\text{Ne}}=0.01$–0.02. Specifically in relation to the problems of the WD cooling rate and of presupernova evolution, we are interested in the radial distribution of Ne, as remarked in Sec. I. According to the BIM analyses described above, chemical separation takes place in C-Ne BIM's ($R_Z=1.67$) at solidification, but not in O-Ne BIM's ($R_Z=1.25$). Thus it is important to investigate how the neon "contaminant" affects a mixture that is predominantly carbon and oxygen.

A similar problem arises with respect to magnesium in an ^{16}O-^{20}Ne-^{24}Mg TIM, as traces $x_{\text{Mg}}\sim0.05$ of Mg have been predicted [4] as an important minor constituent of O-Ne-Mg WD's. Because the value of $R_Z=1.5$ for O-Mg corresponds to the critical value for chemical separation, inclusion of Ne in an O-Mg BIM may reduce the "effective charge ratio" and thereby hinder possible chemical separation of the mixture. In this section,

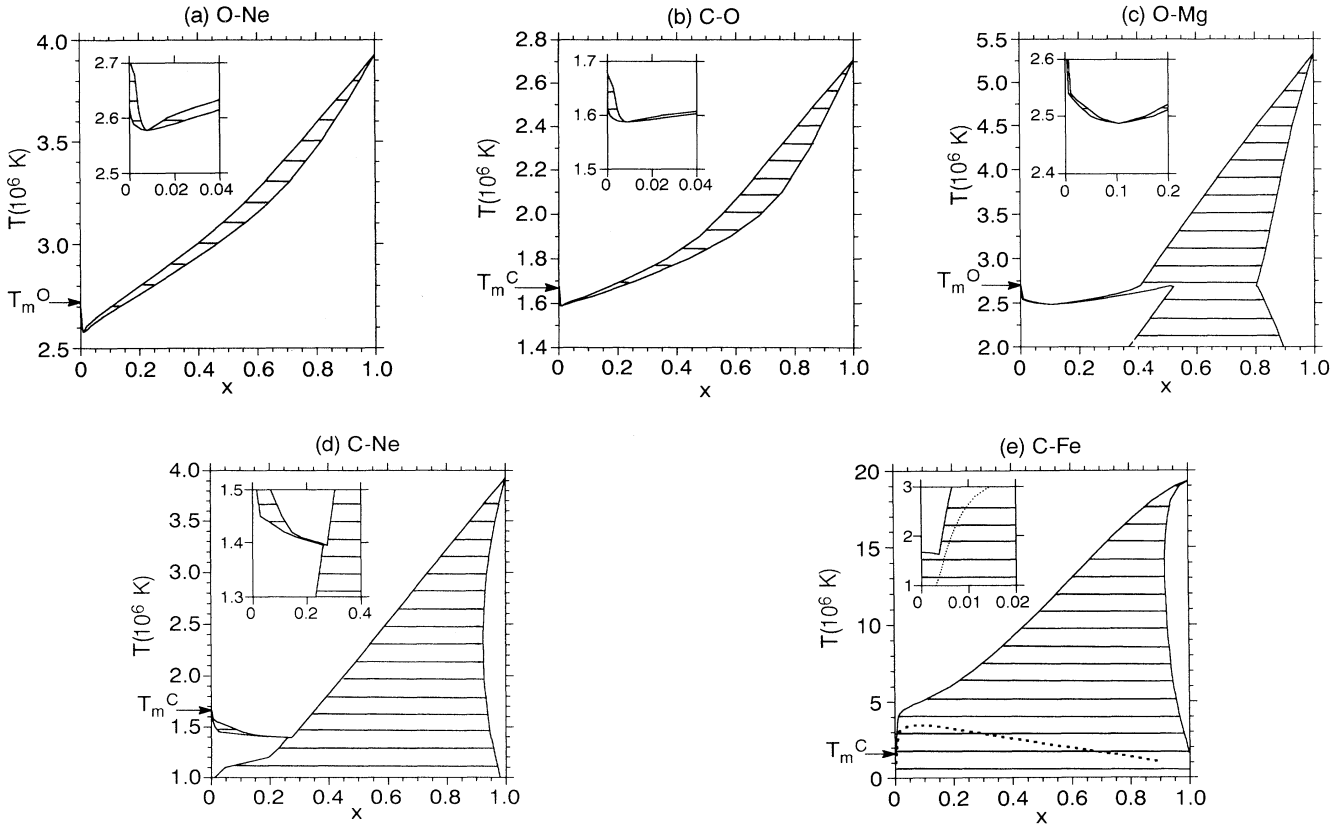

FIG. 7. Phase diagrams for BIM's at $P=10^{22}$ dyn cm^{-2}: (a) O-Ne, (b) C-O, (c) O-Mg, (d) C-Ne, and (e) C-Fe. T_m^i is the freezing temperature for an i-OCP. The dotted curve in panel (e) represents the fluid demixing curve from the bottom panel of Fig. 6.

through numerical analyses of the internal energies and free energies, we demonstrate how solidification may actually proceed in such astrophysically important TIM's.

A. Equations of state

We have calculated the excess internal energies $u_{\rm ex}^{\rm TIM}$ for TIM fluids by the MC simulation method using $N=1200$ particles for $(Z_1,Z_2,Z_3)=(1,2,3)$, (1,2,4), and (1,3,5) for several combinations of x_i and Γ_i. In each run, we have generated 8×10^6 configurations at equilibrium. Table IV lists the computed values for the deviation of $u_{\rm ex}^{\rm TIM}$ from the LM values,

$$\Delta u_{\rm ex}^{\rm TIM}\equiv u_{\rm ex}^{\rm TIM}-x_1u_{\rm ex}^{\rm OCP}(\Gamma_1) -x_2u_{\rm ex}^{\rm OCP}(\Gamma_2)-x_3u_{\rm ex}^{\rm OCP}(\Gamma_3)\ . \tag{39}$$

For the solid phase, we have calculated the Madelung energy $E_M^{\rm TIM}$ in configurations of random-bcc-type at $(Z_1,Z_2,Z_3)=(1,2,4)$, with $N=432$ particles, and the energy is obtained as an average over ten different starts.

TABLE IV. MC results for the normalized excess internal energy $u_{\rm ex}^{\rm TIM}$ and the deviation $\Delta u_{\rm ex}^{\rm TIM}$ from the OCP LM value for various TIM fluids. The quantity $\Delta u_{\rm model}^{\rm TIM}$ is the value obtained from Eq. (41), as described in text.

Z_1	Z_2	Z_3	x_1	x_2	x_3	Γ_1	$u_{\rm ex}^{\rm TIM}$	$\Delta u_{\rm ex}^{\rm TIM}$	$\Delta u_{\rm model}^{\rm TIM}$
1	3	5	$\frac{1}{3}$	$\frac{1}{3}$	$\frac{1}{3}$	10	-63.591 ± 0.002	0.014	0.015
1	2	4	0.5	0.5	0	20	-35.863 ± 0.001	0.007	0.005
1	2	4	0.495	0.495	0.01	20	-37.289 ± 0.001	0.004	0.004
1	2	4	0.6	0.2	0.2	20	-56.645 ± 0.002	0.007	0.007
1	2	4	0.2	0.6	0.2	20	-72.004 ± 0.002	0.009	0.004
1	2	4	$\frac{1}{3}$	$\frac{1}{3}$	$\frac{1}{3}$	20	-83.302 ± 0.002	0.005	0.006
1	2	4	0.2	0.2	0.6	20	-121.258 ± 0.002	-0.001	0.005
1	2	3	$\frac{1}{3}$	$\frac{1}{3}$	$\frac{1}{3}$	30	-91.357 ± 0.002	0.001	0.004

Table V lists the deviations of $E_M^{\rm TIM}$ from the LM values,

$$\frac{\Delta E_M^{\rm TIM}}{N(Z_1e)^2/a_1} \equiv \frac{E_M^{\rm TIM}}{N(Z_1e)^2/a_1} + 0.895\,929(x_1+x_2R_{Z,21}^{5/3}+x_3R_{Z,31}^{5/3}) . \tag{40}$$

Owing to the very large degree of freedom in different possible parametric combinations for the TIM's, it is particularly desirable to obtain an accurate mixing formula for TIM energies using OCP and/or BIM values. Here we adopt the following formula for the mixtures with $Z_3>Z_2>Z_1$, bilinear in x_i, as an approximation relevant for the excess free energies:

$$\Delta f_{\rm ex}^{\rm TIM}(R_{Z,21},R_{Z,31};x_1,x_2,x_3;\Gamma_1) = x_1x_2\Delta f_{12}\left[\frac{x_2}{x_1+x_2}\right]+x_1x_3\Delta f_{13}\left[\frac{x_3}{x_1+x_3}\right] + x_2x_3\Delta f_{23}\left[\frac{x_3}{x_2+x_3}\right] , \tag{41}$$

where the quantities Δf_{ij} are defined by

$$\Delta f_{ij}(x)\equiv\frac{1}{x(1-x)}\Delta f_{\rm ex}^{\rm BIM}(R_{Z,ji},x,\Gamma_i) . \tag{42}$$

Note that Eq. (41) reduces to the BIM formulas in Eqs. (13) or (23) when $x_2=0$, and that it recovers those BIM formulas in the limit $Z_1=Z_2$ or $Z_2=Z_3$ if we ignore residual x dependence in $\Delta f_{ij}(x)$, as expected. In Table IV and V, the excess internal energies calculated from Eq. (41) as $\Delta u_{\rm mode}^{\rm TIM}\equiv\Gamma_1(\partial/\partial\Gamma_1)\Delta f_{\rm ex}^{\rm TIM}$ for the fluid phase and as $\Delta E_{\rm model}^{\rm TIM}/[N(Z_1e)^2/a_1]\equiv[(\partial/\partial\Gamma_1)\Delta f_{\rm ex}^{\rm TIM}]_{T\to0}$ for the solid are listed for comparison with the MC results. We find that Eq. (41) can reproduce the MC energies for both the fluid and solid phases with discrepancies less than or comparable to the standard deviations of the MC values.

To examine the accuracy of Eq. (41) for the fluids at $\Gamma_1\approx1$, we have solved the corresponding HNC equations and have compared the resultant HNC excess free energies $\Delta f_{\rm HNC}^{\rm TIM}$ with Eq. (41). For TIM fluids with $(Z_1,Z_2,Z_3)=(1,2,4)$, we find $(\Delta f_{\rm HNC}^{\rm TIM},\Delta f_{\rm ex}^{\rm TIM})=(0.028,0.027)$ at $(x_1,x_2,x_3)=(\frac{1}{3},\frac{1}{3},\frac{1}{3})$ and $\Gamma_1=1$; (0.037,0.035) at $(\frac{1}{3},\frac{1}{3},\frac{1}{3})$ and 2; (0.022,0.023) at (0.9,0.05,0.05) and 2; (0.007,0.006) at (0.05,0.9,0.05) and 2; and (0.010,0.008) at (0.05,0.05,0.9) and 2. We thus conclude that Eq. (41) maintains its accuracy even at a Γ_1 value as low as unity.

We are primarily interested in determining the free energy when $x_3\ll1$ for both the fluid and solid phases, as this is the parameter range needed for application to C-O-Ne and O-Ne-Mg TIM's in WD interiors. Comparing the internal energies at $(x_1,x_2,x_3)=(0.5,0.5,0)$ and at $(x_1,x_2,x_3)\approx(0.495,0.495,0.01)$ in Tables IV and V, we find that inclusion of the minority "3" particles acts to *decrease* the value of $\Delta u_{\rm ex}^{\rm TIM}$ for the fluid and to *increase* $\Delta E_M^{\rm TIM}$ for the solid; that is,

$$\frac{\partial}{\partial x_3}\Delta f_{\rm ex}^{\rm TIM}\bigg|_{x_3\to0}\begin{cases}<0 & \text{for the fluid}\\ \gtrsim0 & \text{for the solid} .\end{cases} \tag{43}$$

Analogous features have been found for the BIM equations of state, as discussed in Sec. II.

The inequality (43) for the fluid cases can be confirmed independently using a sum-rule argument connecting the BIM screening potentials $H_{ij}(0)$ and the derivatives of $\Delta f_{\rm ex}^{\rm TIM}$, in exact analogy with the sum-rule argument for BIM fluids given in Sec. II A. As in the case of the OCP screening potentials, the quantities $H_{ij}(0)$ correspond to the difference between the excess free energies before and after a nuclear reaction in a BIM. Corresponding to the three possible combinations in the reactions, i.e., $(i,j)=(1,1)$, (1,2), and (2,2), we have the sum rules [cf. Eq. (17)]

$$\frac{\partial}{\partial x_3}\Delta f_{\rm ex}^{\rm TIM}(R_{Z,31}=2)\bigg|_{x_3\to0}\equiv\lim_{\varepsilon\to0}\frac{\partial}{\partial\varepsilon}\Delta f_{\rm ex}^{\rm TIM}(R_{Z,21},2;x_1-(1+x_2)\varepsilon,x_2+x_2\varepsilon,\varepsilon;\Gamma_1) = 2f_{\rm ex}^{\rm OCP}(\Gamma_1)-f_{\rm ex}^{\rm OCP}(\Gamma_3)+\Delta f_{\rm ex}^{\rm BIM}(R_{Z,21},x_2,\Gamma_1)-\frac{H_{11}(0)}{k_bT} , \tag{44a}$$

TABLE V. The deviation of the normalized Madelung energy $\Delta E_M^{\rm TIM}$ for various TIM random solids. The quantity $\Delta E_{\rm model}^{\rm TIM}$ is the value obtained from Eq. (41), as described in text.

Z_1	Z_2	Z_3	x_1	x_2	x_3	$\frac{\Delta E_M^{\rm TIM}}{N(Z_1e)^2/a_1}$	$\frac{\Delta E_{\rm model}^{\rm TIM}}{N(Z_1e)^2/a_1}$
1	2	4	0.5	0.5	0	0.0050±0.000 1	0.0052
1	2	4	0.4954	0.4954	0.0093	0.0051±0.0002	0.0060
1	2	4	0.6019	0.1991	0.1991	0.0039±0.0003	0.0048
1	2	4	0.1991	0.6019	0.1991	0.0079±0.0004	0.0064
1	2	4	$\frac{1}{3}$	$\frac{1}{3}$	$\frac{1}{3}$	0.0074±0.0005	0.0078
1	2	4	0.1991	0.1991	0.6019	0.0141±0.0001	0.0146

$$\left.\frac{\partial}{\partial x_3}\Delta f_{\rm ex}^{\rm TIM}(R_{Z,31}=1+R_{Z,21})\right|_{x_3\to 0}\equiv\lim_{\varepsilon\to 0}\frac{\partial}{\partial\varepsilon}\Delta f_{\rm ex}^{\rm TIM}(R_{Z,21},1+R_{Z,21};x_1-x_2\varepsilon,x_2-x_1\varepsilon,\varepsilon;\Gamma_1)$$
$$=f_{\rm ex}^{\rm OCP}(\Gamma_1)+f_{\rm ex}^{\rm OCP}(\Gamma_2)-f_{\rm ex}^{\rm OCP}(\Gamma_3)+\Delta f_{\rm ex}^{\rm BIM}(R_{Z,21},x_2,\Gamma_1)-\frac{H_{12}(0)}{k_BT}\ , \tag{44b}$$

$$\left.\frac{\partial}{\partial x_3}\Delta f_{\rm ex}^{\rm TIM}(R_{Z,31}=2R_{Z,21})\right|_{x_3\to 0}\equiv\lim_{\varepsilon\to 0}\frac{\partial}{\partial\varepsilon}\Delta f_{\rm ex}^{\rm TIM}(R_{Z,21},2R_{Z,21};x_1+x_1\varepsilon,x_2-(1+x_1)\varepsilon,\varepsilon;\Gamma_1)$$
$$=2f_{\rm ex}^{\rm OCP}(\Gamma_2)-f_{\rm ex}^{\rm OCP}(\Gamma_3)+\Delta f_{\rm ex}^{\rm BIM}(R_{Z,21},x_2,\Gamma_1)-\frac{H_{22}(0)}{k_BT}\ . \tag{44c}$$

Numerical values calculated from Eqs. (44) using Eqs. (6), (13), and (18) are listed in Table VI for various TIM's; for reference, values of $(\partial/\partial x_3)f_{\rm ex}^{\rm TIM}|_{x_3\to 0}$ calculated from Eq. (41) are given in parentheses. For all cases listed in Table VI, the sum-rule values of $(\partial/\partial x_3)f_{\rm ex}^{\rm TIM}|_{x_3\to 0}$ take on negative values, in agreement with the inequality (43) for the fluid phase.

B. Chemical separation at solidification

Inequality (43) leads us to an interesting scenario for the solidification of a TIM fluid with a small molar fraction of "3." (We recall that $x_3=0.01-0.05$ in some of the WD interiors; thus, cases with $x_3\ll 1$ are the astrophysically interesting ones.) For those TIM's, it is reasonable to regard the energy associated with "3" particles as a small perturbation to the total free energy. As the temperature decreases, the TIM thus first produces a solid following the phase diagram for the 1-2 BIM. No "3" particles are to be found in the resulting *solid* because an addition of "3" would act to *increase* $\Delta f_{\rm ex}^{\rm TIM}$ in the solid over that in the fluid, as the inequalities (43) imply. The subsequent evolution of the solidification depends on the details of the 1-2 phase diagrams.

For TIM's with $R_{Z,21}\lesssim 1.4$, including C-O-Ne ($R_{Z,21}=1.33$) and O-Ne-Mg ($R_{Z,21}=1.25$) mixtures, the phase diagrams for 1-2 are of the azeotropic type, and the molar fraction of "2" at the azeotrope, $x_2\sim 0.01$, is smaller than the $x_3=0.01-0.05$ assumed for the WD's. Since the inequality $x_2(\text{solid})>x_2(\text{fluid})$ holds in the BIM azeotropic diagrams, the fraction of "2" in the fluid decreases as solidification proceeds, until the fluid becomes effectively a 1-3 mixture with a small fraction of "2" ($x_2\sim 0.01$). Finally, if $R_{Z,31}\gtrsim 1.6$, the 1-3 mixture forms a (nearly) pure solid of "3," as the BIM phase diagrams imply. We thus conclude that chemical separation of the "3" species occurs at solidification for TIM's with $R_{Z,21}\lesssim 1.4$ and $R_{Z,31}\gtrsim 1.6$ when $x_3\ll 1$.

For ^{12}C-^{16}O-^{22}Ne TIM's in WD's, the charge ratios are $R_{Z,21}=1.33$ and $R_{Z,31}=1.67$ and the molar fraction of "3" is $x_3=0.01-0.02$. Therefore, following the argument given in the preceding paragraph, chemical separation of neon is predicted at solidification. The radial distribution of neon in a WD is in fact determined through comparison of the mass densities of the C-O-Ne fluid and the coexisting C-O solid at phase separation. Solidification in a WD is expected to start from the center, where the mass density and hence the freezing temperature are highest. If the C-O solid produced at the center is lighter than the C-O-Ne fluid, the solid floats up and remelts, thereby reducing the oxygen fraction at the center. In this case, a nearly pure neon core finally forms. If the solid is heavier than the fluid, on the other hand, the same argument leads us to expect a neon-rich layer to be formed gradually in the outer layers of the star.

To determine which of these scenarios one obtains, we compare the mass densities of the C-O solids and the C-O-Ne fluids under WD conditions. The mass-density difference between the two phases at constant pressure is

$$\frac{\rho(\text{solid})-\rho(\text{fluid})}{\rho(\text{fluid})}=\frac{n_e(\text{solid})}{n_e(\text{fluid})}\frac{\mu_e(\text{solid})}{\mu_e(\text{fluid})}-1\ , \tag{45}$$

TABLE VI. Numerical values of $(\partial/\partial x_3)\Delta f_{\rm ex}^{\rm TIM}|_{x_3\to 0}$ for various TIM fluids derived from the sum rules given in Eqs. (44). The numbers in parentheses represent the values calculated from Eq. (41).

$R_{Z,21}$	x_2	Γ_1	$R_{Z,31}=2$	$R_{Z,31}=1+R_{Z,21}$	$R_{Z,31}=2R_{Z,21}$
1.2	0.1	30	−0.67 (−2.20)	−0.79 (−2.39)	−0.92 (−2.57)
1.2	0.5	30	−0.64 (−2.53)	−0.75 (−2.50)	−0.88 (−2.45)
1.2	0.9	30	−0.66 (−2.55)	−0.78 (−2.45)	−0.91 (−2.24)
1.2	0.1	50	−1.14 (−2.23)	−1.34 (−2.43)	−1.56 (−2.61)
1.2	0.5	50	−1.11 (−2.56)	−1.31 (−2.53)	−1.52 (−2.48)
1.2	0.9	50	−1.14 (−2.57)	−1.33 (−2.43)	−1.55 (−2.26)
1.5	0.1	50	−1.14 (−2.19)	−1.64 (−2.45)	−2.25 (−2.63)
1.5	0.5	50	−1.09 (−2.53)	−1.59 (−2.53)	−2.20 (−2.41)
1.5	0.9	50	−1.15 (−2.60)	−1.63 (−2.51)	−2.24 (−2.23)

where n_e is the electron number density for each phase and $\mu_e = \sum_i x_i A_i / \sum_i x_i Z_i$. At constant n_e, the addition of ^{22}Ne to a ^{12}C-^{16}O fluid increases its mass density, since the ratio $A/Z = 2.2$ for neon is larger than the ratio $A/Z = 2$ that holds for both carbon and oxygen. We evaluate Eq. (45) by treating the partial pressures due to the ions as perturbations to the pressure of the relativistically degenerate electrons, in the same way as we did in the construction of the phase diagrams in Sec. II C. To lowest order in the quantity $\delta V/V_0$ of Eq. (38), we then find that Eq. (45) can be approximated as

$$\frac{\rho(\text{solid})-\rho(\text{fluid})}{\rho(\text{fluid})} \approx \frac{\mu_e(\text{solid})}{\mu_e(\text{fluid})} - 1 - \left[\frac{\delta V(\text{solid})}{V_0} - \frac{\delta V(\text{fluid})}{V_0} \right] \frac{\mu_e(\text{solid})}{\mu_e(\text{fluid})} . \tag{46}$$

Figure 8 exhibits the boundaries arising from the condition $\rho(\text{solid}) < \rho(\text{fluid})$ for ^{12}C-^{16}O solids and ^{12}C-^{16}O-^{22}Ne fluids with $x_{\text{Ne}} = 0$ (dotted lines), 0.01 (dashed lines), and 0.02 (solid lines), at the freezing temperature of carbon. In the top panel, the pressure is $P = 4.79 \times 10^{21}$ dyn cm^{-2}, while for the bottom panel it is $P = 5.38 \times 10^{22}$ dyn cm^{-2}. In WD interiors, we may assume [2] $P > 10^{23}$ dyn cm^{-2} and $x_{\text{Ne}} = 0.01$–0.02. Thus we find that ^{12}C-^{16}O solids are lighter than ^{12}C-^{16}O-^{22}Ne fluids for *any* molar fraction of oxygen in the fluid and solid phases assumed for WD's.

To conclude, we predict the formation of a nearly pure neon core upon solidification of a C-O-Ne WD for *any* C:O ratio. For O-Ne-Mg WD's, the same arguments demonstrate the possibility of chemical separation and formation of a nearly pure magnesium core. Significantly increased accuracy in the calculations would be required for a precise determination of the critical value of R_Z at which chemical separation takes place in BIM's.

IV. CONCLUDING REMARKS

In this paper, we have calculated the free energies for BIM fluids with $R_Z \leq 5$ [Eq. (16)] using MC results for the internal energies and the sum rule [Eq. (17)] for the OCP screening potential. For BIM solids with $R_Z \leq 4.5$, we have also evaluated free energies for three types of BIM solid structures [Eqs. (24) and (25)] through a combination of Madelung-energy calculations with internal energies calculated from MC simulations. We find that random solids have the lowest free energy near solidification. From the BIM phase diagrams shown in Figs. 7, constructed with the compressibility of the relativisitically degenerate electrons included, we find that the form of the phase diagram changes as a function of R_Z from an azeotropic type when $R_Z \lesssim 1.5$ to a eutectic type at $R_Z \gtrsim 1.5$. In addition, through a comparison of the MC results for the internal energies and the BIM screening potentials at zero separation via the sum rules in Eqs. (44), we have found an accurate free-energy formula [Eq. (41)] for TIM fluids and solids. We have applied these results for TIM's, specifically using the inequality (43) for the free energy, to C-O-Ne WD's. We predict chemical separation of neon at solidification, and the consequent formation of a nearly pure neon core in such WD's.

One of the most critical problems that remains to be investigated is an examination of the accuracy of Eq. (25) for the entropy of mixing, especially for the random solids. For BIM solids near the solidification temperatures, the magnitude of $\Delta S^{\text{BIM}}/(Nk_B)$ is comparable to that of $\Delta f_{\text{ex}}^{\text{BIM}}$. While $\Delta f_{\text{ex}}^{\text{BIM}}$ has been determined with good accuracy by the MC simulation method, the value of ΔS^{BIM} for random solids given in Eq. (25) remains an assumption. Yet another problem to be investigated is the effect of screening by the relativistically degenerate electrons on the free energies of the ions, an effect neglected in the present study. It has been pointed out [39] that the screening length of the electrons, in units of

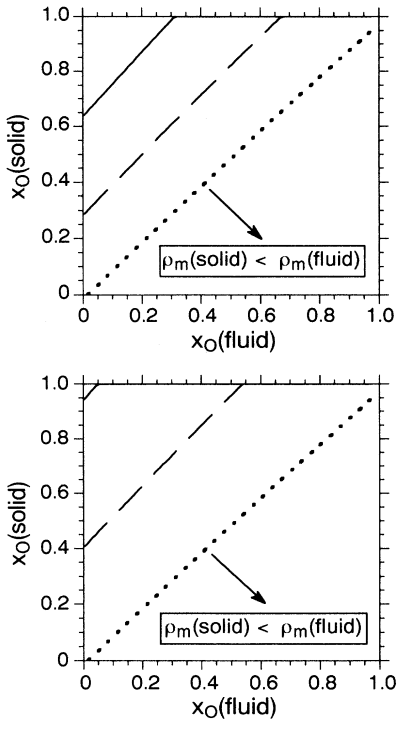

FIG. 8. Comparison of the relative mass densities of ^{12}C-^{16}O solids and ^{12}C-^{16}O-^{22}Ne fluids with $x_{\text{Ne}} = 0$ (dotted curves), 0.01 (dashed curves), and 0.02 (solid curves) at the freezing temperature for carbon. The pressure is $P = 4.79 \times 10^{21}$ dyn cm^{-2} for the top panel and $P = 5.38 \times 10^{22}$ dyn cm^{-2} for the bottom panel. The mass density of the C-O solid is *less* than that of the C-O-Ne fluid in the region *below* each of the curves, as indicated by the arrow.

the ion-sphere radius, remains finite even in the limit of high densities. Because the permissible errors of the excess free energies must be $\lesssim 0.1\%$ in order to be useful for calculations of phase diagrams, it is possible that such electron-screening effects may have non-negligible consequences for the free energies and phase diagrams.

ACKNOWLEDGMENTS

We are grateful to Dr. K. Nomoto for useful discussions and comments. This research was supported in part by Grants-in-Aid for Scientific Research provided by the Ministry of Education, Science, and Culture of Japan through Research Grant Nos. 04455010 and 1387, and in part by the U.S. National Science Foundation under Grant No. INT90-16293 through the University of Rochester. This work was also funded in part by the Japan–U.S. Cooperative Science Program: *Phase Transitions in Dense Astrophysical Plasmas,* supported jointly by the Japan Society for the Promotion of Science and the U.S. National Science Foundation. One of us (H.M.V.H.) also wishes to thank Dr. H. E. DeWitt for discussions of the Madelung energies of BIM solids at zero temperature.

[1] S. Ichimaru, Rev. Mod. Phys. **54**, 1017 (1982).
[2] F. D'Antona and I. Mazzitelli, Ann. Rev. Astron. Astrophys. **28**, 139 (1990).
[3] E. Anders and N. Grevesse, Geochim. Cosmochim. Acta **53**, 197 (1989).
[4] K. Nomoto and M. Hashimoto, Phys. Rep. **163**, 13 (1988).
[5] W. L. Slattery, G. D. Doolen, and H. E. DeWitt, Phys. Rev. A **26**, 2255 (1982).
[6] S. Ogata and S. Ichimaru, Phys. Rev. A **36**, 5451 (1987).
[7] D. H. E. Dubin, Phys. Rev. A **42**, 4972 (1990).
[8] D. J. Stevenson, J. Phys. (Paris) Colloq. Suppl. **41**, C2-61 (1980).
[9] B. Brami, J.-P. Hansen, and F. Joly, Physica A **95**, 505 (1979).
[10] S. Ichimaru, H. Iyetomi, and S. Ogata, Astrophys. J. **334**, L17 (1988).
[11] J. L. Barrat, J.-P. Hansen, and R. Mochkovitch, Astron. Astrophys. **199**, L15 (1988).
[12] D. E. Winget, C. J. Hansen, J. W. Liebert, H. M. Van Horn, G. Fontaine, R. E. Nather, S. O. Kepler, and D. Q. Lamb, Astrophys. J. **315**, L77 (1987).
[13] J. Isern, R. Mochkovitch, E. Garcia-Berro, and M. Hernanz, Astron. Astrophys. **241**, L29 (1991).
[14] Z. W. Xu and H. M. Van Horn, Astrophys. J. **387**, 662 (1992).
[15] K. Nomoto, Astrophys. J. **277**, 791 (1984).
[16] K. Nomoto, Astrophys. J. **322**, 206 (1987).
[17] S. E. Woosley and T. A. Weaver, Ann. Rev. Astron. Astrophys. **24**, 205 (1986).
[18] E. E. Salpeter, Aust. J. Phys. **7**, 373 (1954).
[19] S. Ogata, S. Ichimaru, and H. M. Van Horn, Astrophys. J. (to be published).
[20] S. Ichimaru, Rev. Mod. Phys. **65**, 255 (1993).
[21] S. Ogata, H. Iyetomi, and S. Ichimaru, Astrophys. J. **372**, 259 (1991).
[22] H. Iyetomi, S. Ogata, and S. Ichimaru, Phys. Rev. B **40**, 309 (1989).
[23] S. Ichimaru, H. Iyetomi, and S. Tanaka, Phys. Rep. **149**, 91 (1987).
[24] B. Widom, J. Chem. Phys. **39**, 2803 (1963).
[25] B. Jancovici, J. Stat. Phys. **17**, 357 (1977).
[26] See, e.g., S. Ichimaru, *Statistical Plasma Physics* (Addison-Wesley, Menlo Park, CA, 1992), Vol. I, Sec. 1.3.
[27] See, e.g., L. L. Foldy, Phys. Rev. B **17**, 4889 (1978).
[28] S. G. Brush, H. L. Sahlin, and E. Teller, J. Chem. Phys. **45**, 2102 (1966).
[29] J.-P. Hansen, Phys. Rev. A **8**, 3096 (1973).
[30] H. L. Helfer, R. L. McCrory, and H. M. Van Horn, J. Stat. Phys. **37**, 577 (1984).
[31] C. Kittel, *Solid State Physics,* 5th ed. (Wiley, New York, 1976), p. 21.
[32] W. L. Press, B. P. Flannery, S. A. Teukolsky, and W. T. Vetterling, *Numerical Recipes "Fortran Version"* (Cambridge University Press, Cambridge, 1989), p. 301.
[33] S. Ichimaru, S. Ogata, and H. M. Van Horn, Astrophys. J. **401**, L35 (1992).
[34] H. Iyetomi and S. Ichimaru, Phys. Rev. A **45**, 437 (1992).
[35] J.-P. Hansen and I. R. McDonald, *Theory of Simple Liquids,* 2nd ed. (Academic, London, 1986), Chap. 5.
[36] J. L. Barrat, M. Baus, and J.-P. Hansen, Phys. Rev. Lett. **56**, 1063 (1986).
[37] E. E. Salpeter, Astrophys. J. **134**, 669 (1961).
[38] A. Kovetz, D. Q. Lamb, and H. M. Van Horn, Astrophys. J. **174**, 109 (1972).
[39] S. Ichimaru and S. Ogata, Astrophys. J. **374**, 647 (1991).